Astron. Astrophys. 340, 203–215 (1998)

ASTRONOMY AND ASTROPHYSICS

# Energy and momentum deposition in coronal holes

## Solar coronal hole simulations compared with interpretations of Yohkoh SXT observations

**K. Tziotziou**[1], **P.C.H. Martens**[2], **and A.G. Hearn**[1]

[1] Sterrekundig Instituut, Postbus 80000, 3508 TA Utrecht, The Netherlands (A.G.Hearn@astro.uu.nl)
[2] SOHO Project, ESA Space Science Department at Goddard Space Flight Center, Code 682.3, Greenbelt, MD 20771, USA

Received 5 January 1998 / Accepted 27 July 1998

**Abstract.** A grid of 74 coronal models with parameterized heating distribution, representing a wide range of physical parameters, has been calculated. We find that three of these models reproduce the recent observations made by Hara et al. (1994) with the soft X-ray telescope aboard the Japanese satellite *Yohkoh*, which indicate a temperature of $1.8 \sim 2.4 \times 10^6$ K with an emission measure of $10^{25.5}$ to $10^{26.2}$ cm$^{-5}$, while other solutions reproduce the more standard *Yohkoh* and Skylab observations, which have a temperature of about $1.4 \times 10^6$ K

The best fit for the coronal temperature and emission measure gives a velocity at the Earth's orbit of only $10\,\mathrm{km\,s^{-1}}$. A model including acceleration by Alfvén waves gives a final velocity of $630\,\mathrm{km\,s^{-1}}$ which is in agreement with the observations. The mechanical heating flux at the transition region is $2.1 \times 10^5\,\mathrm{erg\,cm^{-2}\,s^{-1}}$ with a weighted average dissipation scale length of $0.1\,\mathrm{R_\odot}$. The flux of Alfvén waves is $1 \times 10^5\,\mathrm{erg\,cm^{-2}\,s^{-1}}$.

In our models the velocity of the solar wind from coronal holes is completely determined by the Alfvén wave acceleration, in contrast to previous models in which the Alfvén wave acceleration increased the velocity of the purely thermal model only by a factor 2.

Observations of the non thermal broadening of the coronal red and green lines are consistent with this model.

**Key words:** hydrodynamics – methods: numerical – stars: coronae – stars: mass loss

### 1. Introduction

Coronal holes are extended, long-lived features in the solar corona which are conspicuous in X-ray photographs of the Sun because of the low X-ray emission in comparison with surrounding regions. Coronal holes have open, mainly radial magnetic fields and they are the source of the fast solar wind (Krieger et al. 1973, Nolte et al. 1976).

The work presented in this paper was stimulated by recent soft X-ray observations of coronal holes with the Japanese Yohkoh satellite. The launch of Yohkoh (Ogawara et al. 1991) started a new era in soft X-ray observations of the Sun. The soft X-ray telescope (SXT) of Yohkoh has a spectral range of $3 - 45$Å and its X-ray mirror has much lower scattering wings than the Skylab SO-54 telescope (Tsuneta et al. 1991). This ensures a much more accurate determination of temperatures of coronal holes.

A coronal hole located near the centre of the Sun's disc was observed on 21st March 1992 with the thin aluminium filter of the SXT aboard Yohkoh (Hara et al. 1994). This coronal hole extended into the northern and southern hemispheres. It appeared in January 1992 and lasted until June 1992. During that time it showed almost rigid rotation. It was located in a large magnetic cell with negative polarity and its intensity difference with the surrounding active regions reached three orders of magnitude. Hara et al. (1994) analysed the data and estimated the temperature in the coronal hole to be $1.8 \sim 2.4 \times 10^6$ K with an emission measure of $10^{25.5 \sim 26.2}$ cm$^{-5}$. The temperature derived by Hara et al. from Yohkoh data is much higher than any previous measurements based on Skylab data and is almost the same as that of quiet regions.

In contrast to the results of Hara et al. , Foley et al. (1997), using data from the same experiment (SXT), recently found temperatures in a coronal hole of the order of $1.4 \times 10^6 K$, very similar to the earlier Skylab results. Foley et al. use SXT observations of the north polar coronal hole, for which there is very little contribution from high latitude activity centers. They find that the number of photons from mirror scattering is substantially larger than the signal from the coronal hole itself, but nevertheless their model matches very well the calculated limb profile from the Withbroe (1988) model, albeit at a three times smaller density. It is beyond the scope of this paper to try to resolve this discrepancy in interpretation of observations. We will show in the remainder of this paper that some of models in our grid reproduce the lower temperature corona very well, and are consistent with earlier, stationary, models. The novel aspect of our calculations is that we can also reproduce the coronal wind parameters for a hotter type of coronal hole, as suggested by the results of Hara et al. .

*Send offprint requests to*: A.G. Hearn

Coronal holes are the source of the fast streams in the solar wind. The latest observations of the solar wind were obtained with the solar wind plasma experiment aboard the Ulysses spacecraft. During its first southern polar pass (peak southerly latitude of $-80.2^\circ$ on 13 September 1994 at a heliocentric distance of $2.29$ AU) Ulysses measured most of the physical properties of the solar wind emerging from the south polar coronal hole of the Sun. These observations measured a wind velocity ranging from $700\,\mathrm{km\,s^{-1}}$ to $800\,\mathrm{km\,s^{-1}}$ – the same as measurements at the Earth's orbit – and a mass loss and density at $1$ AU of $\sim 3\times10^{-14}\,\mathrm{M_\odot\,yr^{-1}}$ and $\sim 10^{-23}\,\mathrm{gr\,cm^{-3}}$ respectively (Phillips et al. 1995). The measured magnetic field at the highest southern latitude reached by Ulysses is $\sim 1.5\times10^{-5}\,\mathrm{G}$ (Balogh et al. 1995). Recently Ko et al. (1997) studied the same Ulysses SWICS data. They assumed that the charge states of the heavy ions observed near the spacecraft are frozen in from the inner coronal region, and used these to constrain the temperatures, densities, and velocities in the inner coronal region. Their best fits ($\chi^2\approx3$) yield a maximum coronal hole temperature of $1.4\times10^6K$ to $1.6\times10^6K$, between 1.3 and 1.5 solar radii from the surface. This is consistent with the models of Withbroe (1988), and the results of Foley et al. (1997). However, a maximum temperature of $1.8\times10^6K$ (as in Hara et al. ) leads to $\chi^2\approx4$, which is not much less probable.

The thermal driving mechanism suggested by Parker (1958, 1965) cannot explain the high-speed solar wind, and an additional acceleration mechanism for the solar wind is needed. After the observation of high-amplitude Alfvén waves in the solar wind near the Earth with Mariner V by Belcher & Davis (1971), Belcher (1971) and Alazraki & Couturier (1971) suggested that undamped Alfvén waves could accelerate the solar wind by direct transfer of momentum from the waves to the solar wind flow. Jacques (1977, 1978) made a more extensive study of Alfvén wave pressure in one fluid models of the solar wind. Hartmann & MacGregor (1980, 1982) suggested Alfvén wave pressure as a driving mechanism for winds from late-type giants.

In this paper we treat the heating of the corona (which is a result of dissipation of mechanical energy) and acceleration of the wind as two separate processes by introducing a parameterised mechanical flux for the heating of the corona and an Alfvén wave pressure force, exerted by undamped Alfvén waves on the flow for the acceleration of the solar wind. This gives quantitative estimates for the mechanical heating and acceleration by Alfvén waves needed for a coronal hole model that corresponds with the observations.

A complete study of the temperature, density and velocity structure of the corona has been made by Withbroe (1988). He based his study on the stationary stellar wind models calculated by Hammer (1982a,1982b,1983). Withbroe studied the heating of the lower corona below $10\,\mathrm{R_\odot}$ by dissipation of a mechanical flux with a constant dissipation scale length and the acceleration of the solar wind up to $1$ AU by a flux of Alfvén waves and compared his results with the observations. He used an iterative method to solve the equations by demanding that the solutions go through the critical point with boundary conditions that the temperature and pressure at infinity go to zero. His study used the X-ray observations before Yohkoh , and his models had a temperature of about 1.4 million K, consistent with the more recent results, discussed above, of Foley et al. (1997), and Ko et al. (1997).

In Sect. 2 we discuss previous corona models and observations. Sect. 3 gives a description of our physical model and the numerical method. We present the assumptions, the physical processes that we consider and we review the properties of Alfvén wave pressure on a one-fluid model. We describe the relevant equations for our numerical study and the numerical method we use and we discuss the influence of strong source terms in time-dependent calculations. All the results for the model without and with Alfvén acceleration are presented in Sect. 4.

## 2. Previous corona models and observations

The study of coronal holes in soft X-rays started with images taken by a soft X-ray telescope aboard a sounding rocket. Krieger et al. (1973) used these X-ray data and several simple coronal models to define the physical conditions at the base of the corona and to identify corona holes as the source of the high velocity solar wind stream. They derived a temperature of $1.3\times10^6\,\mathrm{K}$ from the intensity scale height. Maxson & Vaiana (1977) used broad band filter soft X-ray images from Skylab to determine a range of coronal holes temperatures ($9\times10^5\,\mathrm{K}-3\times10^6\,\mathrm{K}$) and emission measures ($5\times10^{26}\,\mathrm{cm^{-5}}-2\times10^{25}\,\mathrm{cm^{-5}}$). This is the same method as employed by Hara et al. (1994). Because of severe scattering due to the mirror micro-roughness, the spectra taken by the soft X-ray telescopes aboard Skylab could not give definite information about temperatures.

Information about coronal holes has also been obtained by observations of EUV lines. The first coronal hole models of Munro & Withbroe (1972) based on EUV data (in the wavelength range of 300-1400 Å) from the Harvard College Observatory (HCO) experiment on OSO-4 gave a temperature of $10^6\,\mathrm{K}$ or less, almost $40\%$ lower than the temperature determined for the quiet Sun. Analysis of EUV spectra recorded by the NRL slit spectrograph aboard Skylab indicated a temperature of less than $10^6\,\mathrm{K}$ and an outflow velocity near the base of the coronal hole of $\sim 20\,\mathrm{km\,s^{-1}}$ (Doschek & Feldman 1977). Mariska (1978) used EUV observations of the lithium-like ions from the Harvard instrument to obtain a temperature and density model for the inner corona of a polar coronal hole. This model gave a temperature of $\sim 1.1\times10^6\,\mathrm{K}$, an electron density of $\sim 1.7\times10^8\,\mathrm{cm^{-3}}$ and an outflow velocity of $15\,\mathrm{km\,s^{-1}}$ just above the base of the corona. For the models based on EUV spectral analysis, lines sensitive to temperatures in the range of $1\times10^6\,\mathrm{K}$ such as Si VIII (1446 Å), Fe X (6374 Å) and Fe XI (1467 Å) have been used. All these models give lower temperatures and densities in the coronal holes than quiet regions and give little information about the heating processes in coronal holes.

The physical properties of the solar wind are known from in situ measurements either with space probes or satellites near the Earth. For reviews of the solar wind the reader is referred to Pneuman (1986), Hundhausen (1977) and Holzer (1979). The association of the solar wind with coronal holes was well established even before the investigation of EUV and X-ray data of the Skylab mission. The observations showed that the solar wind consists of electron, protons and heavy ions (mainly alpha particles). The solar wind velocity at 1 AU varies between $300\,\mathrm{km\,s^{-1}}$ up to $800\,\mathrm{km\,s^{-1}}$ in the high-speed streams. The average temperature of the wind and the magnetic field strength at 1 AU are about $2\times10^5$ K and $3.5\times10^{-5}$ G respectively. Extrapolation of the magnetic field strength observed at 1 AU gives a magnetic field at the coronal base of $\sim 10$ G. The energy flux in the coronal base is estimated to be a few $10^5\,\mathrm{erg\,cm^{-2}\,s^{-1}}$.

## 3. Physical model and numerical method

### *3.1. Physical model and equations*

We assume spherical symmetry, truncated to a cone to represent a coronal hole. The magnetic field is assumed to be radial and enters the calculations only through the Alfvén wave pressure term which is described in Sect. 3.2. The energetics of the flow is described by four different processes: losses by radiation from the gas, heating of the gas by photospheric radiation and by the dissipation of a mechanical energy flux at the base of the corona and heating or cooling by thermal conduction. There is also a force exerted on the flow by gravity and in the model with Alfvén acceleration by the gradient of the Alfvén wave pressure. In the later model, we assume a flux of undamped Alfvén waves that propagate outwards in an accelerating medium.

Stationary solutions for coronal holes are obtained by solving the time dependent equations. We use a rather arbitrary temperature distribution at the beginning of the calculation of stationary corona models but in most cases the last calculated coronal model is used for the start of a new set of parameters.

The equations solved are the Euler equations for an ideal compressible flow with spherical symmetry in the conserved form

$$\frac{\partial}{\partial t}\boldsymbol{w}+\frac{\partial}{\partial r}\boldsymbol{f}(\boldsymbol{w})=\boldsymbol{s}(r,\boldsymbol{w}) \tag{1}$$

where $\boldsymbol{w}$, $\boldsymbol{f}$ and $\boldsymbol{s}$ represent the vectors of the conserved quantities, fluxes and source terms.

These equations are the continuity equation, the momentum equation, the energy equation and an equation for state given by

$$\frac{\partial}{\partial t}\rho+\frac{1}{r^2}\frac{\partial}{\partial r}\left(r^2\rho v\right)=0 \tag{2}$$

$$\frac{\partial}{\partial t}\rho v+\frac{1}{r^2}\frac{\partial}{\partial r}\left(r^2(\rho v^2+p)\right)=-\rho g+\frac{2p}{r}+\mathcal{F}_{\rm alv} \tag{3}$$

$$\frac{\partial}{\partial t}e+\frac{1}{r^2}\frac{\partial}{\partial r}\left(r^2v(e+p)\right)=-\rho v g+Q_{\rm tot}+v\mathcal{F}_{\rm alv} \tag{4}$$

$$p=\rho\frac{\mathcal{R}T}{\mu} \tag{5}$$

where $r$ is the radial distance from the centre of the star, $\rho$ the gas density, $v$ the radial velocity, $p$ the gas pressure, $T$ the temperature, $\mathcal{R}$ the gas constant, $\mu$ equal to 0.5 the mean molecular weight for a fully ionized hydrogen gas, $\gamma=5/3$ the ratio of specific heats and $\mathcal{F}_{\rm alv}$ is the force due to Alfvén waves. The total energy density $e$ is defined as

$$e=\frac{1}{2}\rho v^2+\frac{p}{\gamma-1} \tag{6}$$

and

$$g=\frac{GM_\star}{r^2} \tag{7}$$

is the gravitational acceleration where $G$ is the gravitational constant and $M_\star$ the mass of the star.

$Q_{\rm tot}$ is the sum of all external energy sources

$$Q_{\rm tot}=Q_{\rm op}+Q_{\rm rad}+Q_{\rm cond}+Q_{\rm mech} \tag{8}$$

where $Q_{\rm op}$ represents the opacity heating of the gas because of absorption of photospheric radiation, $Q_{\rm rad}$ the radiation losses, $Q_{\rm cond}$ the thermal conduction and $Q_{\rm mech}$ the mechanical heating.

The radiation losses and the opacity heating are defined by

$$Q_{\rm rad}=-\rho^2P_{\rm rad}(T) \tag{9}$$

$$Q_{\rm op}=W_{\rm d}(r)\rho^2P_{\rm op}(T) \tag{10}$$

where $P_{\rm rad}(T)$ is the radiation loss function (McWhirter et al. 1975, 1977) and $W_{\rm d}(r)$ the dilution factor. Fig. (1) gives the form of the radiation loss function $P_{\rm rad}(T)$ calculated for the mass density instead of the electron density. $P_{\rm op}(T)$ is the equivalent opacity heating function that contains contributions from the bound-free and free-free opacities of hydrogen and depends on the effective temperature $T_{\rm eff}$ of the star.

The conductive heating $Q_{\rm cond}$ is

$$Q_{\rm cond}=\nabla\cdot(K_{\rm o}T^{5/2}\nabla T)=\frac{1}{r^2}\frac{\partial}{\partial r}\left(r^2K_{\rm o}T^{5/2}\frac{\partial T}{\partial r}\right) \tag{11}$$

where $K_{\rm o}$ is the conduction coefficient which depends only logarithmically on density (Spitzer 1956). For typical coronal densities $K_{\rm o}\approx10^{-6}\,\mathrm{erg\,cm^{-1}\,s^{-1}\,K^{-7/2}}$. This is valid only if the mean free path of the electrons, which are responsible for the heat conduction, is less than the temperature scale height. We introduce a limiter in the calculation of the conductive flux which ensures that electrons do not have to move faster than the electron thermal speed to carry the conductive flux.

Mechanical heating $Q_{\rm mech}$ is by dissipation of sawtooth waves of specified frequency $\nu$ calculated from weak shock-wave theory (Ulmschneider 1970)

$$Q_{\rm mech}=\nu(\gamma+1)\left(\frac{12F_{\rm mech}^3}{\gamma pc^3}\right)^{\frac{1}{2}} \tag{12}$$

where

$$c=\left(\gamma\frac{p}{\rho}\right)^{\frac{1}{2}} \tag{13}$$

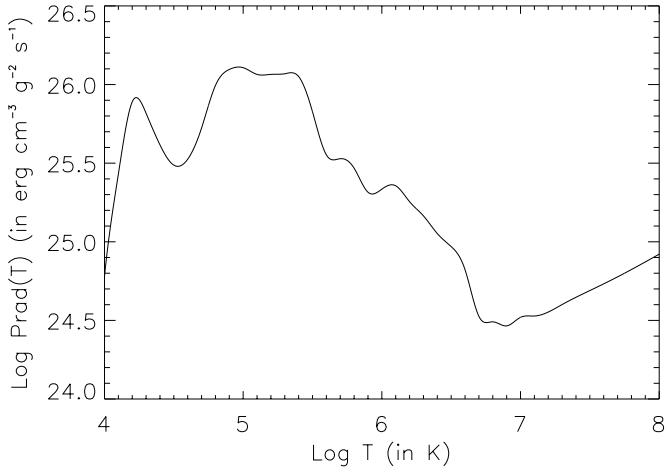


**Fig. 1.** The radiation loss function $P_{\rm rad}(T)$ calculated by McWhirter et al. as a function of temperature.

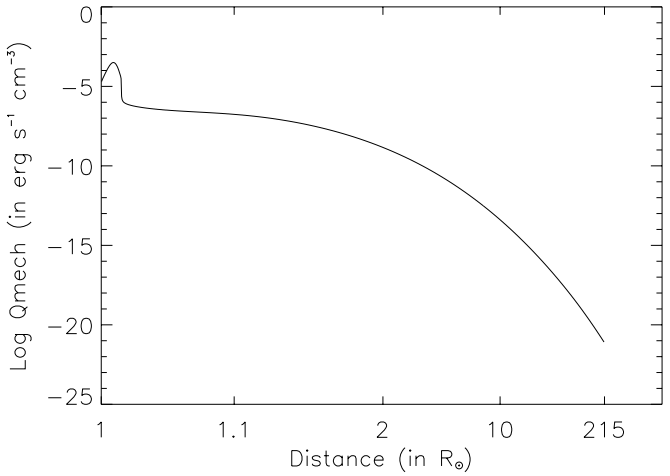


**Fig. 2.** The mechanical flux $Q_{\rm mech}$ as a function of heliocentric distance for a flux at the base of the calculation of $F_{\rm o} = 1.28 \times 10^7$ erg cm$^{-2}$ s$^{-1}$ and a wave period of 500 sec. This is for model **C**, which is the fit to the results of Hara et al. .

is the adiabatic velocity of sound and $F_{\rm mech}$ is the flux of mechanical energy. This mechanical heating should be considered as a parameterised quantity with no further physical interpretations attached to it. One specific advantage of this particular form of parameterisation is that it gives stable stationary solutions in the time dependent calculations while a simple dissipation length for the mechanical heating does not. Fig. 2 shows the form of this parameterised heating as a function of distance. Since the calculations start in the photosphere of the star ($r = 1\,{\rm R}_\odot$) the important parameter is not the mechanical flux at the bottom of the numerical grid but the flux entering the transition zone. A large fraction of the mechanical heating flux is quickly dissipated within a few stellar radii from the surface of the star.

### *3.2. Alfvén wave pressure*

The force exerted on the flow by the propagating Alfvén waves is the gradient of the Alfvén wave pressure. An extensive discussion of Alfvén wave pressure has been given by Jacques (1977, 1978). We assume Alfvén waves propagating outwards in a magnetic field varying as

$$B = B_{\rm o}\left(\frac{r_{\rm o}}{r}\right)^2 \tag{14}$$

where $r_{\rm o}$ is the radius of the star and $B_{\rm o}$ is the magnetic field at the surface of the star. The Alfvén wave force $\mathcal{F}_{\rm alv}$ in the momentum equation (Eq. (3)) is then equal to

$$\mathcal{F}_{\rm ext} = -\nabla\cdot\mathbf{P}_{\rm w} = -\frac{1}{2}\frac{{\rm d}\mathcal{E}}{{\rm dr}} \tag{15}$$

where $\mathbf{P}_{\rm w}$ is the wave stress tensor and $\mathcal{E}$ is the energy density of the Alfvén waves.
The components of the wave tensor $\mathbf{P}_{\rm w}$ have been calculated by Dewar (1970) but in the case of Alfvén waves propagating radially along the background magnetic field the wave tensor becomes (Jacques 1977)

$$\mathbf{P}_{\rm w} = \frac{1}{2}\mathcal{E}\mathbf{I} \tag{16}$$

where $\mathbf{I}$ is the unity tensor. The energy density $\mathcal{E}$ is equal to

$$\mathcal{E} = \frac{\delta B^2}{8\pi} = \frac{1}{2}\rho(\delta v_{\rm A})^2 \tag{17}$$

where $\delta B$ (or equivalently $\delta v_{\rm A}$) is the amplitude of the Alfvénic fluctuations.
The associated wave energy flux $\boldsymbol{F_{\rm A}}$ for Alfvén waves with group velocity $\boldsymbol{v_{\rm g}}$ is

$$\boldsymbol{F_{\rm A}} = \boldsymbol{v_{\rm g}}\mathcal{E} + \boldsymbol{v}\cdot\mathbf{P}_{\rm w} \tag{18}$$

where $\boldsymbol{v}$ is the velocity of the flow. For Alfvén waves with propagation vectors $\boldsymbol{k}$ parallel to the flow velocity $\boldsymbol{v}$ the dispersion relation is

$$\omega = k(v + v_{\rm A}) \tag{19}$$

where

$$v_{\rm A} = \frac{B}{\sqrt{(4\pi\rho)}} \tag{20}$$

is the Alfvén speed. The group velocity is then

$$v_{\rm g} = \frac{\partial\omega}{\partial k} = v + v_{\rm A} \tag{21}$$

When there are velocity gradients in the flow the wave energy is not conserved. If there is no dissipation then the wave energy equation for an expanding atmosphere is (Jacques 1977)

$$\frac{\partial\mathcal{E}}{\partial t} + \nabla\cdot\boldsymbol{F_{\rm A}} = \boldsymbol{v}\cdot\nabla\cdot\mathbf{P}_{\rm w} \tag{22}$$

This shows that in an accelerating medium the wave energy is not conserved because of the interaction between the flow and

the waves (right hand side of the equation). An analysis shows that for undamped Alfvén waves in an accelerating flow the conserved quantity is the wave action density $S$ defined as

$$S = \frac{\mathcal{E}}{\omega_{\rm o}} = \frac{\mathcal{E}}{\omega - kv} \tag{23}$$

Wave action is an adiabatically conserved quantity (Dewar 1970, Bretherton 1970). Consider a wave with a frequency $\omega$ and an energy density $\mathcal{E}$ running on a background medium at rest. In a Galilei transformation in a reference frame moving with constant velocity $v$ parallel to the wave vector $k$ the Doppler effect causes a lowering of the observed frequency to $\omega - kv$ and a corresponding decrease in wave energy. In a given volume the number of wave packets is still the same, since volume is invariant under Galilei transformations. A measure of this number of wave packets is the wave action $S = \mathcal{E}/\omega_{\rm o}$. Conservation of wave action is equivalent to the conservation of wave quanta. In the absence of dissipation, wave action determines the amplitude of the waves as a function of heliocentric distance. The conservation law for wave action $S$ is

$$\frac{\partial S}{\partial t} + \nabla \cdot (\boldsymbol{v_{\rm g}} S) = 0 \tag{24}$$

Integration of Eq. (24) gives

$$\frac{(v_{\rm A} + v)^2 r^2 \mathcal{E}}{v_{\rm A}} = const \tag{25}$$

From Eqs. (18), (21) we obtain

$$F_{\rm A} = \left(\frac{3}{2} v + v_{\rm A}\right) \mathcal{E} \tag{26}$$

Finally combining Eqs. (25), (26) gives

$$\mathcal{E}(r) = const \frac{v_{\rm A}}{(v + v_{\rm A})^2 r^2} \tag{27}$$

with

$$const = \frac{(v_{\rm A_o} + v_o)^2 r_{\rm o}^2 F_{\rm A_o}}{v_{\rm A_o}(\frac{3}{2} v_{\rm o} + v_{\rm A_o})} \tag{28}$$

where $v_{\rm o}$, $v_{\rm A_o}$, and $F_{\rm A_o}$ are the velocity, the Alfvén velocity and the Alfvén flux respectively at the base of the calculation.
The value of $\mathcal{E}$ in our calculations is derived from the conservation of wave action for undamped Alfvén waves. That is true as long as $\delta B/B < 1$. If the magnetic field perturbation $\delta B$ in the wave becomes comparable with the background field $B$ then the solution is no longer physical. This condition is satisfied by requiring that $\delta B/B < 1$, which means that the wave energy $\mathcal{E}$ is smaller than the energy density $\mathcal{E}_{\rm B} = B^2/8\pi$ of the background magnetic field. This can be done approximately by letting $\mathcal{E}$ be given by Eq. (27) if $\mathcal{E} < \mathcal{E}_{\rm B}$ and $\mathcal{E} = \mathcal{E}_{\rm B}$ if $\mathcal{E} \geqq \mathcal{E}_{\rm B}$.

### *3.3. The numerical method*

Our numerical simulations of coronal holes solve Eqs. (2) - (4) using a hydrodynamic code developed by Korevaar & Van Leer (1988). This code is a one dimensional time dependent numerical code. It is based on an implicit conservative upwind method using Van Leer's differentiable flux-splitting (Van Leer 1982).

The numerical scheme is first-order in time but second-order in space. The radially symmetric grid extends from the photosphere of the star up to a distance equal to the distance of Earth from the Sun and it has more grid points in the inner parts of the corona including the transition region and the photosphere. The boundaries are transparent allowing waves and flows to pass through them without being reflected back into the numerical grid. These non-reflecting boundaries are achieved by extrapolating the physical variables inside and outside the numerical grid using the characteristic variables (for definition see Sect. 3.4). Most attention has been paid to the inner boundary which lies in the dense photosphere. The outer boundary, where the flow is supersonic in most calculations, can usually be ignored. The timestep $\Delta t$ of the calculations is directly related to the convergence of the numerical calculations to the stationary solution. When the solution is close to the stationary solution then the timestep becomes very large and the implicit time dependent method turns into a Newton-Raphson iteration.

When a new set of computational parameters is defined, a converged solution satisfying the physics of the flow is reached within some 15000 time steps. The runs have been performed with a DEC Alpha/400 workstation and a stationary solution requires about half an hour.

### *3.4. Calculations with strong source terms*

In this section we discuss the effect in time dependent calculations of strong source terms, that is source terms with very large gradients. Kelly & Korevaar (1995) studied numerically the case of a Type II supernova with the same hydrodynamic code in which they introduced a strong source term due to the gradient of radiation pressure. They have shown that in the case of a very strong source term it is better to solve the equations of momentum and energy in the conservative form of Eq. (1) with no gradients present as source terms. This is achieved by including in the flux vector $\boldsymbol{f}$ of Eq. (1) the flux associated with the gradient of the new source term. In the case of a strong Alfvén pressure gradient that would mean that Eqs. (3), (4) should be rewritten in the form

$$\frac{\partial}{\partial t}\rho v + \frac{1}{r^2}\frac{\partial}{\partial r}\left(r^2(\rho v^2 + p + P_{\rm w})\right) = -\rho g + \frac{2(p + P_{\rm w})}{r} \tag{29}$$

$$\begin{aligned}\frac{\partial}{\partial t}(e + 2P_{\rm w}) \; + \; & \frac{1}{r^2}\frac{\partial}{\partial r}\left(r^2 v(e + 2P_{\rm w} + p + P_{\rm w})\right) \\ & = -\rho v g + Q_{\rm tot}\end{aligned} \tag{30}$$

where $P_{\rm w}$ is the Alfvén pressure given by Eq. (16). The new conservative quantity would be now $e + 2P_{\rm w}$, the sum of the energy density $e$ given by Eq. (6) and the energy density of the Alfvén waves $\mathcal{E} = 2P_{\rm w}$. Kelly & Korevaar (1995) have shown that the numerical results achieved with the use of Eqs."(29), (30) are more accurate than the results achieved by solving Eqs. (3), (4)

which contain the large Alfvén wave pressure gradient $-\nabla P_{\rm w}$ as a source term.

The time dependent calculations using the momentum and energy equations in the conservative form of Eqs. (29), (30) are less straightforward than in the study of the Type II supernova because of the more complicated form of the Alfvén wave pressure gradient. The complication arises from the calculation of the characteristic variables $\boldsymbol{q}$ (Hirsch 1990, Heyvaerts 1996) of the flow. Their introduction ensures that the one-dimensional Euler equations (see Eq. (1)) can be decoupled in the $\boldsymbol{q}$ variables. This set of quantities is defined by the relation

$$d\boldsymbol{q} = \boldsymbol{R}^{-1} d\boldsymbol{w} \tag{31}$$

where $\boldsymbol{R}$ consists of the right eigenvectors of $\partial \boldsymbol{f}/\partial \boldsymbol{w}$. Characteristic variables have been introduced because they ensure the calculation of well behaved gradients of the auxiliary variables of gas pressure $p$ and sound speed $c$. These auxiliary variables in the presence of shocks during the second-order scheme are not treated as conserved quantities. For simple hydrodynamical flows the calculation of the characteristic variables is easy, but in a flow with an Alfvén wave pressure gradient it is almost impossible because of the direct dependence of $P_{\rm w}$ on $r$.

So for the calculations with the Alfvén wave pressure we will still use Eqs. (3), (4) and the energy density $e$ as the conserved quantity. The results will be less accurate but the global picture will not change significantly.

## 4. Results

### *4.1. Coronal hole models without Alfvén wave pressure*

Stationary coronal models have been calculated for a grid of parameters without Alfvén wave pressure. The calculations have two input parameters which uniquely define the solution, the flux $F_{\rm o}$ of waves at the base of the calculation in the photosphere and their period $P$. For each solution the temperature, density and velocity is calculated as a function of radial distance. A grid of 74 coronal models has been calculated.

Table 1 gives the maximum coronal temperature of the solutions for the computational parameters $F_{\rm o}$ and $P$. There are thirteen simulations that result not in a stationary solution but in an corona undergoing a global relaxation oscillation. The existence of such a global relaxation oscillation had first been proposed by Hearn et al. (1983) and has been studied numerically by Korevaar & Hearn (1989b).

Table 2 shows the emission measure $EM$ calculated for the stationary solutions. The emission measure $EM$ is given by

$$EM = \int_{1{\rm R}_\odot}^{1{\rm AU}} N_{\rm e}^2(\ell) {\rm d}\ell \tag{32}$$

where $N_{\rm e}$ is the number density of electrons and $\ell$ is the path length along the line of sight. For this integral we consider only temperatures above $5 \times 10^5$ K.

The interpretation of the Yohkoh observations by Hara et al. , under the assumption of isothermal emission along the line of sight, gave a mean temperature in the range of 1.8 to 2.4 $10^6$ K and an emission measure in the range of $10^{25.5}$ to $10^{26.2}$ cm$^{-5}$. Only three of our coronal models give a maximum temperature and emission measure within this range. Since the temperature profile is very flat in all cases, the average emission measure weighted temperature is normally only slightly lower than the maximum temperature, so a comparison with these three models is meaningful. (Models that have a maximum temperature below the range determined by Hara et al. are obviously excluded). These three solutions are very close to the relaxation oscillations and they are marked in Tables 1 and 2 with bold face numbers. Table 3 shows these three models and they are rather similar. The important physical parameters, the flux of energy and pressure at the transition region, differ by less than a factor of 2. Only one of these models which fits the Yohkoh data is discussed further and that is Model **C** which gives the best fit within the range of the Yohkoh results.

Fig. 2 shows the mechanical heating $Q_{\rm mech}$ (in units of erg cm$^{-3}$ s$^{-1}$) as a function of distance. The dissipation scale length $L$ which is not constant can locally be calculated by

$$\frac{1}{r^2 F_{\rm mech}} \frac{\Delta(r^2 F_{\rm mech})}{\Delta r} = -\frac{1}{L} \tag{33}$$

where $F_{\rm mech}$ (in erg cm$^{-2}$ s$^{-1}$) is the rate of mechanical energy input in the corona. If there is no dissipation $r^2 F_{\rm mech}$ remains constant. Fig. 3 shows the dissipation scale length as a function of heliocentric distance. The dissipation length in the photosphere is coupled to the density scale height. The bulk of the mechanical energy is dissipated before it reaches the transition region. In this model $98\%$ of the mechanical flux $F_{\rm o}$ of $1.28 \times 10^7$ erg cm$^{-2}$ s$^{-1}$ is dissipated in the photosphere and only $2\%$ enters the transition region for heating the corona. The weighted average dissipation scale length in the corona using the mechanical flux as a weighting function is $0.1\,{\rm R}_\odot$.

Figs. (4) and (5) show the temperature and density profiles for model **C**. The density of $10^{-8}$ gr cm$^{-3}$ at the base of the photosphere drops rapidly in the transition region because the temperature is rising rapidly at constant pressure. The temperature increases rapidly to one million K. It reaches its maximum value of $1.9 \times 10^6$ K at a distance of $0.14\,{\rm R}_\odot$ above the transition region and then starts dropping slowly to $2 \times 10^4$ K at $215\,{\rm R}_\odot$ (1 A.U). This is one order of magnitude lower than the measured temperature of the solar wind at the orbit of the Earth. The calculated emission measure (Eq. (32)) is $10^{25.83}$ cm$^{-5}$ and the average weighted temperature along the line of sight using the emission measure as the weight function is $1.7 \times 10^6$ K.

Fig. 6 shows the velocity profile of the flow. The velocity at the Earth's radius is subsonic and about $10$ km s$^{-1}$. This is a very slow wind, very different from the $700$ km s$^{-1}$ observed near the orbit of Earth. The wind does become supersonic eventually. The critical point is at $1714\,{\rm R}_\odot$. The reason for the low velocity wind is that the heating of the corona occurs in the inner corona. The outer regions of the corona are heated by thermal conduction from the region of temperature maximum. With the densities of the outer corona the energy supplied by thermal conduction is insufficient to accelerate the flow to high velocities.

**Table 1.** Maximum temperature (in $10^6$ K) of the calculated stationary solutions for different values of base flux $F_o$ and wave period $P$. There are 13 simulations (here noted with R.O) which give a global relaxation oscillation. The bold face numbers indicate the coronal models which fit the Yohkoh data.

| Wave period (in sec) | Base Wave flux $F_o$ (in $10^5$ erg cm$^{-2}$ s$^{-1}$) | | | | | | | | |
|---|---|---|---|---|---|---|---|---|---|
| | 1 | 2 | 4 | 8 | 16 | 32 | 64 | 128 | 256 |
| 400 | | 1.0 | 1.1 | 1.2 | 1.3 | 1.4 | 1.5 | 1.5 | |
| 500 | 1.1 | 1.2 | 1.3 | 1.4 | 1.6 | 1.7 | **1.8** | **1.9** | R.O |
| 1000 | 1.4 | 1.6 | **1.8** | R.O | R.O | R.O | R.O | R.O | R.O |
| 2000 | 1.6 | 1.8 | 2.1 | R.O | R.O | R.O | R.O | R.O | R.O |
| 4000 | 1.7 | 1.9 | 2.2 | 2.5 | 2.9 | 3.4 | 4.1 | 5.0 | |
| 8000 | 1.8 | 2.1 | 2.4 | 3.0 | 3.6 | 4.4 | 5.5 | 6.9 | |
| 16000 | 2.1 | 2.4 | 2.9 | 3.4 | 4.2 | 5.2 | 6.5 | 8.3 | |
| 32000 | 2.3 | 2.7 | 3.2 | 4.0 | 5.0 | 6.0 | 7.4 | 9.4 | |
| 64000 | 2.7 | 3.1 | 3.8 | 4.5 | 5.6 | 6.9 | 8.6 | 10.6 | |

**Table 2.** Log of Emission Measure (in cm$^{-5}$) of the calculated stationary solutions for different values of base flux $F_o$ and wave period $P$. There are 13 simulations (here noted with R.O) that give a global relaxation oscillation. The bold face numbers indicate the coronal models which fit the Yohkoh data.

| Wave period (in sec) | Base Wave flux $F_o$ (in $10^5$ erg cm$^{-2}$ s$^{-1}$) | | | | | | | | |
|---|---|---|---|---|---|---|---|---|---|
| | 1 | 2 | 4 | 8 | 16 | 32 | 64 | 128 | 256 |
| 400 | | 25.01 | 25.07 | 25.31 | 25.34 | 25.37 | 25.59 | 25.60 | |
| 500 | 24.97 | 25.05 | 25.30 | 25.34 | 25.57 | 25.60 | **25.61** | **25.83** | R.O |
| 1000 | 25.03 | 25.28 | **25.51** | R.O | R.O | R.O | R.O | R.O | R.O |
| 2000 | 25.00 | 25.23 | 25.44 | R.O | R.O | R.O | R.O | R.O | R.O |
| 4000 | 24.91 | 24.93 | 25.08 | 25.07 | 25.05 | 25.20 | 25.39 | 25.50 | |
| 8000 | 24.62 | 24.63 | 24.78 | 24.79 | 24.95 | 25.09 | 25.27 | 25.45 | |
| 16000 | 24.35 | 24.52 | 24.54 | 24.71 | 24.90 | 25.05 | 25.23 | 25.41 | |
| 32000 | 24.25 | 24.30 | 24.48 | 24.53 | 24.71 | 24.97 | 25.23 | 25.46 | |
| 64000 | 24.04 | 24.23 | 24.30 | 24.48 | 24.66 | 24.84 | 25.02 | 25.31 | |

**Table 3.** The three stationary solutions that best fit the Yohkoh observations. $F_o$ is the wave base flux, $P$ is the period of the waves, $T_{max}$ is the maximum temperature, EM the emission measure, $F_{tr}$ the flux entering the transition region, $\dot{M}$ the mass loss, $p_{tr}$ the gas pressure at the transition region and $v_{wind}$ the solar wind velocity at the orbit of the Earth.

| Quantity | Units | Stationary Solution | | |
|---|---|---|---|---|
| | | **A** | **B** | **C** |
| P | sec | 1000 | 500 | 500 |
| $F_o$ | erg cm$^{-2}$ s$^{-1}$ | $4 \times 10^5$ | $6.4 \times 10^6$ | $1.28 \times 10^7$ |
| $F_{tr}$ | erg cm$^{-2}$ s$^{-1}$ | $1.31 \times 10^5$ | $1.53 \times 10^5$ | $2.12 \times 10^5$ |
| $T_{max}$ | K | $1.8 \times 10^6$ | $1.8 \times 10^6$ | $1.9 \times 10^6$ |
| EM | cm$^{-5}$ | $10^{25.51}$ | $10^{25.61}$ | $10^{25.83}$ |
| $\dot{M}$ | $M_\odot$ yr$^{-1}$ | $2.5 \times 10^{-14}$ | $1.4 \times 10^{-14}$ | $1.9 \times 10^{-14}$ |
| $p_{tr}$ | dyne cm$^{-2}$ | $2.9 \times 10^{-2}$ | $3.4 \times 10^{-2}$ | $4.6 \times 10^{-2}$ |
| $v_{wind}$ | km s$^{-1}$ | 16 | 13 | 5 |

Model **C** gives a good fit with the Yohkoh observations for coronal temperature and emission measure but the velocity of the solar wind at the Earth's orbit is very low. It must be emphasized here that this model of a coronal hole is very different from the models that fit the earlier observations of coronal holes which suggested a maximum coronal temperature of about 1.4 million K. This difference shows that acceleration by Alfvén waves is needed to provide almost all the acceleration to high velocities and not just to give a modest increase in the final solar wind velocity.

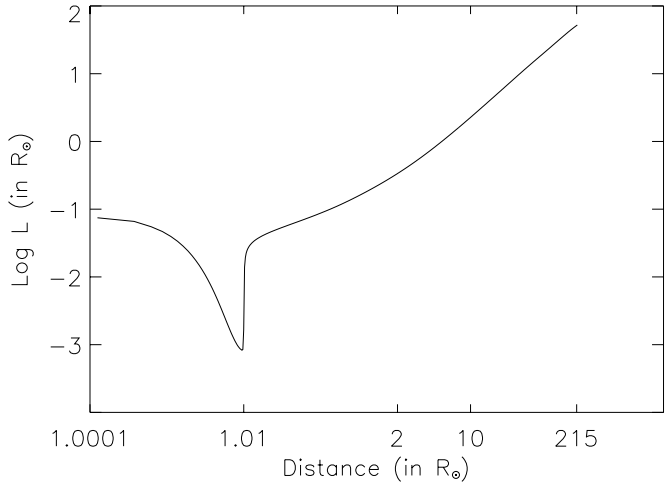


**Fig. 3.** The dissipation scale length L (in $R_\odot$) of the mechanical heating as a function of heliocentric distance for the stationary solution **C**.

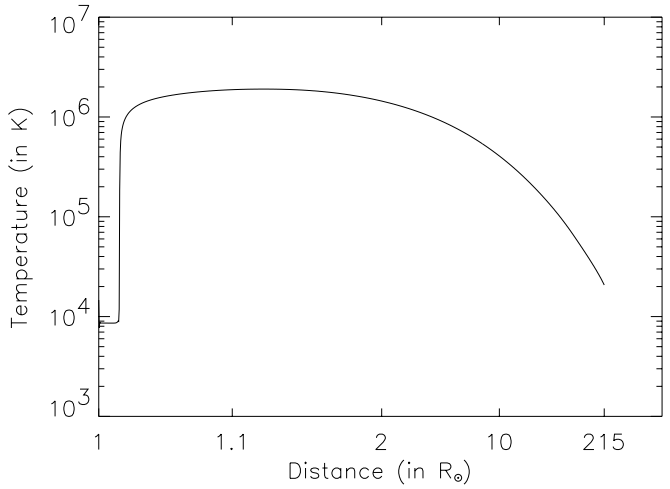


**Fig. 4.** The temperature T (in K) as a function of heliocentric distance for the stationary solution **C**.

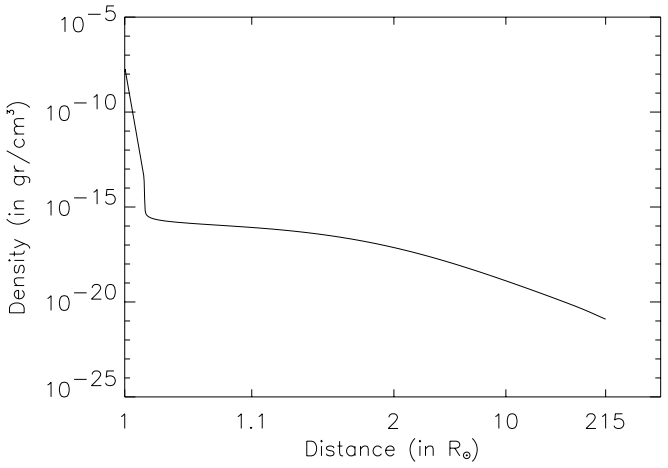


**Fig. 5.** The density $\rho$ (in $\mathrm{gr\,cm^{-3}}$) as a function of heliocentric distance for the stationary solution **C**.

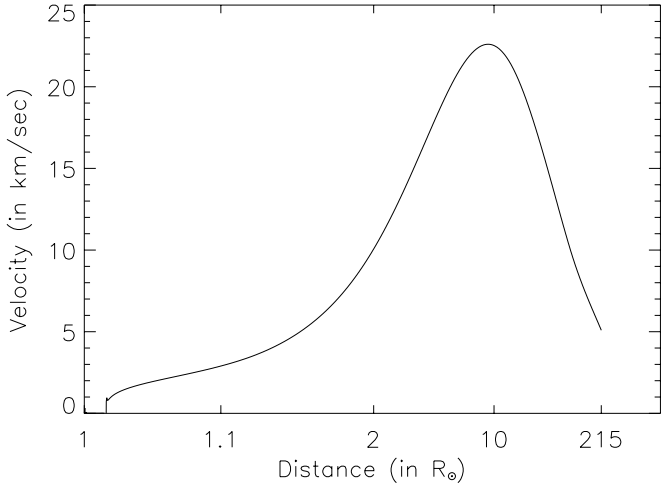


**Fig. 6.** The velocity v (in $\mathrm{km\,s^{-1}}$) of the solar wind as a function of heliocentric distance for the stationary solution **C**.

### *4.2. Simulations with Alfvén wave pressure*

In this section Model **C**, which gives the best fit to the Yohkoh observations, is modified to include the acceleration of the solar wind by Alfvén waves. The contribution of Alfvén waves to the momentum and energy equations has already been given in Sect. 3.2. The accelerating force due to the Alfvén wave pressure gradient is

$$\begin{aligned}\mathcal{F}_{\rm alv} &= -\frac{1}{2}\frac{\mathrm{d}\mathcal{E}}{\mathrm{d}r} \\ &= -\frac{1}{2}\frac{(v_{\rm A_o}+v_o)^2 r_{\rm o}^2 F_{\rm A_o}}{v_{\rm A_o}(\frac{3}{2}v_{\rm o}+v_{\rm A_o})}\frac{\mathrm{d}}{\mathrm{d}r}\left(\frac{v_{\rm A}}{(v+v_{\rm A})^2 r^2}\right) \end{aligned} \quad (34)$$

where $\mathcal{E}$ is the energy density of the Alfvén waves, $v$ the flow velocity, $v_{\rm A}$ the Alfvén velocity and $F_{\rm A_o}, v_{\rm o}, v_{\rm A_o}$ are the Alfvén flux, flow velocity and Alfvén velocity at the base of the corona.

In this calculation the magnetic field at the surface of the star is 10 G and the Alfvén wave flux at the surface of the star is $1\times10^5\,\mathrm{erg\,cm^{-2}\,s^{-1}}$. The magnetic field is assumed to be purely radial.

Figs. (7)-(9) show the results obtained including the Alfvén wave acceleration in the calculations. We present the average profiles of temperature, density and velocity as a function of heliocentric distance of the last 200000 timesteps of our numerical simulations. With the inclusion of the Alfvén wave acceleration the Euler equations are not solved in their conservative form. This is discussed in Sect. 3.4. In the outer regions of the corona (above 5 $R_\odot$) where the Alfvén wave force is dominant, there is a continuous creation of small numerical shocks which do not allow the numerical simulation to relax fully into a stationary solution. For this reason physical quantities are averaged over the last 200000 timesteps.

From the equation of motion

$$\rho\frac{\mathrm{d}\boldsymbol{v}}{\mathrm{d}t} = -\nabla p + \rho\boldsymbol{g} + \boldsymbol{\mathcal{F}_{\rm ext}} \quad (35)$$

**Table 4.** Properties of the two calculated models, without and with the Alfvén wave acceleration as described in Sects. 4.1 and 4.2 and their corresponding values according to observations and previous models.

| Quantity | Model without Alfvén pressure | Model with Alfvén pressure | Observations and previous models | |
|---|---|---|---|---|
| Base mechanical flux $F_o$ | $1.28 \times 10^7$ erg cm$^{-2}$ s$^{-1}$ | $1.28 \times 10^7$ erg cm$^{-2}$ s$^{-1}$ | | |
| Mechanical flux $F_{tr}$ [$\alpha$] | $2 \times 10^5$ erg cm$^{-2}$ s$^{-1}$ | $2 \times 10^5$ erg cm$^{-2}$ s$^{-1}$ | few $10^5$ erg cm$^{-2}$ s$^{-1}$ | [1] |
| Alfvén base flux $F_{A_o}$ | none | $1 \times 10^5$ erg cm$^{-2}$ s$^{-1}$ | few $10^5$ erg cm$^{-2}$ s$^{-1}$ | [1] |
| Magnetic field $B_o$ at 1 $R_\odot$ | none | 10 G | $\sim 10$ G | [2] |
| Pressure $p_{tr}$ [$\beta$] | $4.6 \times 10^{-2}$ dyne cm$^{-2}$ | $4.2 \times 10^{-2}$ dyne cm$^{-2}$ | $2.2 \times 10^{-2}$ dyne cm$^{-2}$ | [3] |
| Maximum Temperature $T_{max}$ | $1.9 \times 10^6$ K | $1.7 \times 10^6$ K | $1.8 \sim 2.4 \times 10^5$ K | [4] |
| Distance of $T_{max}$ | 1.14 $R_\odot$ | 1.14 $R_\odot$ | | |
| Distance of sonic point | none [$\delta$] | 10 $R_\odot$ | $\sim 7 - 10$ $R_\odot$ | [5] |
| Wind velocity v at 1 AU | 5 km s$^{-1}$ | 630 km s$^{-1}$ | $\sim 700 - 800$ km s$^{-1}$ | [6] |
| Density $\rho$ at 1 AU | $1.2 \times 10^{-21}$ gr cm$^{-3}$ | $1.3 \times 10^{-23}$ gr cm$^{-3}$ | $\sim 10^{-23}$ gr cm$^{-3}$ | [6] |
| Temperature T at 1 AU | $2 \times 10^4$ K | $2 \times 10^4$ K | $2 \times 10^5$ K | [7] |
| Mass loss $\dot{M}$ | $1.9 \times 10^{-14}$ $M_\odot$ yr$^{-1}$ | $2.9 \times 10^{-14}$ $M_\odot$ yr$^{-1}$ | $\sim 3 \times 10^{-14}$ $M_\odot$ yr$^{-1}$ | [6] |
| Emission measure EM | $10^{25.83}$ cm$^{-5}$ | $10^{25.79}$ cm$^{-5}$ | $10^{25.5 \sim 26.2}$ cm$^{-5}$ | [4] |
| Average temperature $T_{av}$ [$\gamma$] | $1.7 \times 10^6$ K | $1.5 \times 10^6$ K | | |

[$\alpha$] $F_{tr}$ is the mechanical flux through the transition region
[$\beta$] $p_{tr}$ is the pressure at the transition region
[$\gamma$] $T_{av}$ is the averaged temperature with the emission measure as a weight function
[$\delta$] The flow is subsonic up to 1 AU. The sonic point lies at r = 1714 $R_\odot$
[1] Model values. See Withbroe (1988)
[2] Inferred by Skylab observations and models. See Hundhausen (1977)
[3] Value inferred by EUV observations and models. See Munro & Withbroe (1972)
[4] Yohkoh observations. See Hara et al. (1994)
[5] There are no observations. The value depends on the model considered.
[6] Ulysses observations. See Phillips et al. (1995)
[7] Inferred by several in situ observations.

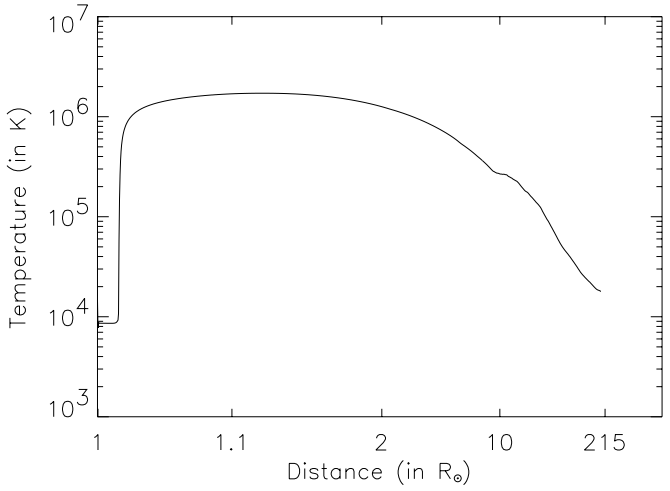


**Fig. 7.** The average profile (over 200000 timesteps) of the temperature T (in K) as a function of heliocentric distance for the Alfvén wave pressure model.

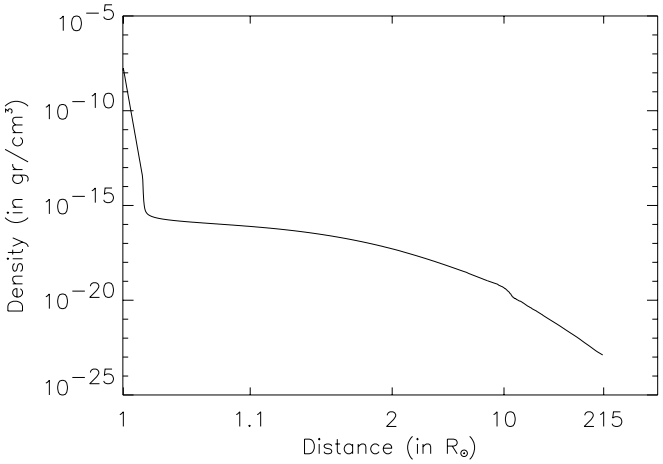


**Fig. 8.** The average profile (over 200000 timesteps) of the density $\rho$ (in gr cm$^{-3}$) as a function of heliocentric distance for the Alfvén wave pressure model.

it is obvious that the extra acceleration depends on how large the Alfvén wave and thermal pressure forces outward are compared with gravity inwards. Fig. 10 shows the absolute value of the three forces acting on the flow averaged over the last 200000 timesteps. Very close to the surface of the star, in the transition region and in the inner corona, the outward forces are close to the inward force of gravity. In the outer regions of corona the Alfvén wave force dominates leading to rapid acceleration. The physical properties of the coronal model close to the star

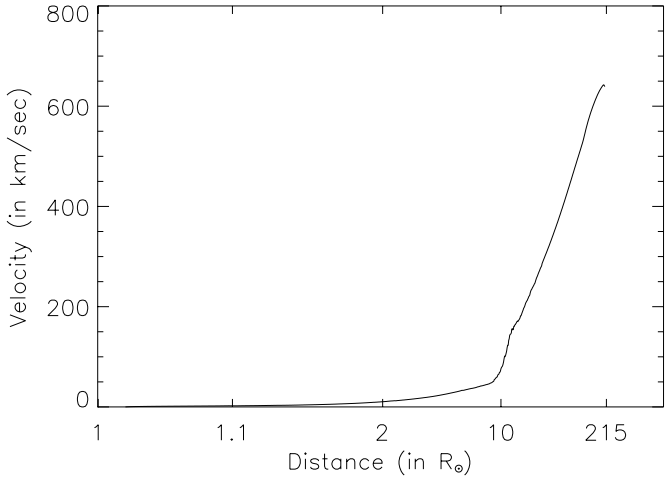


**Fig. 9.** The average profile (over 200000 timesteps) of the wind velocity (in $\mathrm{km\,s^{-1}}$) as a function of heliocentric distance for the Alfvén wave pressure model.

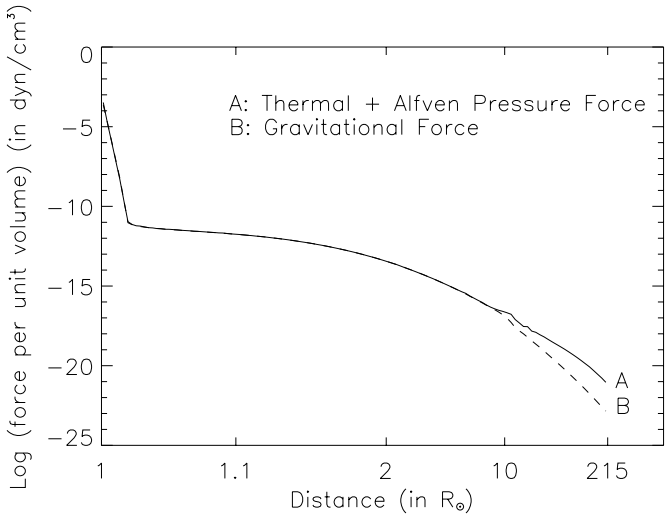


**Fig. 10.** The averaged forces per unit volume acting on the flow for the model with Alfvén acceleration. The dashed line represents the absolute value of the gravitational force per unit volume and the solid line represents the sum of the thermal pressure and Alfvén wave pressure force per unit volume.

are not significantly different from the coronal model without Alfvén wave acceleration. In the outer regions of the corona the force due to Alfvén waves dominates and the velocity increases substantially.

Table 4 shows the main properties of Model **C** without and with Alfvén wave acceleration and results derived from other observations and models. The model with Alfvén wave acceleration is in good agreement with the observations. Including the Alfvén wave acceleration changes the velocity of the solar wind at the Earth's orbit from $5\,\mathrm{km\,s^{-1}}$ to 630 $\mathrm{km\,s^{-1}}$. This is slightly less than the observations. This difference could be resolved with extra fine tuning of the Alfvén wave flux.
The Alfvén wave flux used in this model of $10^5\,\mathrm{erg\,cm^{-2}\,s^{-1}}$ at the base of the corona, is quite modest. With this flux the amplitude of the Alfvén waves in the photosphere would be 8 $\mathrm{km\,s^{-1}}$, which is quite consistent with the upper limit imposed by observations.

## 5. Discussion

An interesting physical question is why our simulations with higher ($\approx 1.8$ million K) temperatures require additional acceleration of the outer regions of the corona by Alfvén waves to reproduce the observed fast solar wind speed at 1 AU, while the solutions with lower maximum temperatures (of the order of 1.4 million K) do not. The physical mechanism behind this has been explored in detail for stellar coronae by Hearn & Vardavas (1981). We summarize this mechanism as follows. An enhanced thermal energy input leads to a corona with a higher maximum temperature and a higher total mass and average density. This is borne out by all coronal models that we are aware of. The higher density in the regions beyond the temperature maximum leads to higher radiative loss from there. Beyond the region of significant thermal energy input (i.e. beyond several dissipation lengths) this energy must be provided by thermal conduction. A higher conductive flux requires a higher temperature gradient in the region beyond the temperature maximum and hence the temperature decreases more rapidly with height than in comparable models with less thermal energy input. A lower temperature in the outer regions of the corona leads to a sonic point that is further removed from the stellar surface and a lower critical velocity. Hence the final velocity of the stellar wind is lower than in comparable model with lower thermal energy input.

Our models that yield a maximum temperature in the corona of $\approx 1.8$ million K constitute an extreme example of the above effect: the sonic point lies at 1714 solar radii, far beyond 1 AU, and the wind velocity at 1 AU is only 10 km/sec. Hearn & Vardavas (1981) found from their stationary numerical solutions that as the thermal energy input is increased slightly in these extreme cases, the temperature in the outer layers decreases even further, resulting in increased radiative energy losses, and even greater demands on the conductive energy supply. Eventually this leads to catastrophic collapse of the outer layers of the corona, and a stationary solution is no longer possible. Hearn et al. (1983) predicted that the corona would then start a relaxation oscillation, slowly building up in mass and temperature until a catastrophic cooling collapse leads to a thin hot corona at the base, and cool and tenuous outer layers. This was confirmed in fully time dependent numerical simulations by Hearn & Korevaar (1989b).

Our present grid of simulations confirms the above results for the Solar corona: we find relaxation oscillations when the thermal energy input surpasses a certain threshold. The models with a corona with a maximum temperature of $\approx 1.8$ million K appear to be very close to that threshold – a slight increase in base flux is sufficient to destroy the stationary solution, as Table 2 bears out. Any models that do not reproduce this result, for example by assuming a constant temperature in the outer layers of the corona from the onset, simply miss an essential ingredient of the physics.

Hence we have found the seemingly contradictory result that solar coronal hole models with higher energy input and higher temperatures than inferred from Skylab observations, require additional wave acceleration in the outer layers to reproduce the observed wind velocities at 1 AU.

Another method to study the physical conditions in the solar corona is from the intensity ratio of the coronal red line (Fe X 6374 Å) and the green line (Fe XIV 5303 Å). These lines are from forbidden transitions and can be observed by ground based coronographs in very bright coronal regions or very close to the limb. Guhathakurta et al. (1992) derived from this intensity ratio a temperature of $1.3 - 1.4 \times 10^6$ K at $1.15\,\mathrm{R}_\odot$ by assuming that the same temperature structures are seen in both emission lines. An analysis of the line widths of the red and green coronal lines observed out to $1.16\,\mathrm{R}_\odot$ with the NSO/Sacramento Peak Observatory Coronograph (Hasler & Moran 1994) suggested a large component of non-thermal broadening, increasing with height and ranging from $40$ to $60\,\mathrm{km\,s^{-1}}$ depending upon the assumed temperature. The total observed Gaussian widths (both thermal and non-thermal components) range from $34$ to $62\,\mathrm{km\,s^{-1}}$. These observations are extremely useful in the context this work since they strongly suggest the presence of hydromagnetic waves that could heat and accelerate the solar wind.

The 1/e Gaussian line width $\delta v$ (in $\mathrm{km\,s^{-1}}$) is defined as

$$\delta v = \frac{\Delta\lambda}{\lambda} c = \sqrt{\delta v_{\rm th}^2 + \delta v_{\rm A}^2} \tag{36}$$

where $\delta v_{\rm A}$ is the amplitude of the Alfvénic fluctuations, which can be calculated by solving Eqs. (17), (27) and (20), $\delta v_{\rm th}$ is the velocity of the thermal fluctuations, $c$ is the velocity of light and $\Delta\lambda$ (in Å) is the observed 1/e Gaussian width of a line of wavelength $\lambda$. The velocity $\delta v_{\rm th}$ is

$$\delta v_{\rm th} = \sqrt{\frac{2kT}{m_{\rm a}}} \tag{37}$$

where $k$ is the Boltzmann constant, $T$ the temperature and $m_{\rm a}$ the mass of the atom, in this case an atom of Fe.

Fig. 11 shows the line width calculated from model **C** including Alfvén waves using Eq. (36). The thermal broadening, the broadening from the Alfvén wave flux, and the combined broadening are plotted as a function of height in solar radii. In addition the total line broadening deduced from two different observations by Hassler & Moran (1994) are plotted. The calculated line width increases with height from 28 $\mathrm{km\,s^{-1}}$to 38 $\mathrm{km\,s^{-1}}$. The observed widths vary from 34 to 62 $\mathrm{km\,s^{-1}}$. Given the uncertainties in the model, the theoretical results are consistent with the coronal line width observations, although there appears to be a systematic trend of increasing line-width with height in the observations, that is absent in our model.

The theoretical model with Alfvén wave acceleration agrees very well with the inner corona observations of Hara et al. . The model explains the velocity of the solar wind at the orbit of the Earth but fails to explain the temperature. The observed temperature is $2 \times 10^5$ K whereas the model gives $2 \times 10^4$ K which is the same as the temperature in the model without Alfvén wave

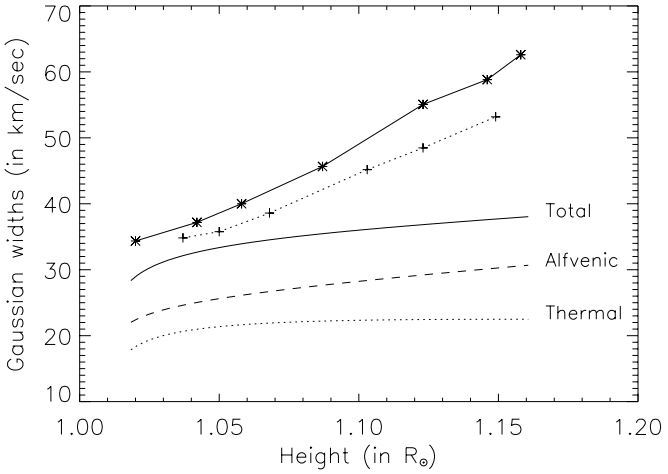


**Fig. 11.** Calculated and observed line widths of Fe X (6374 Å) (in $\mathrm{km\,s^{-1}}$) as a function of height, assuming a Gaussian fit. The dotted line represents the calculated width due to the thermal component, the dashed line the calculated width due to the Alfvénic component and the solid line the sum of the two components. The other two lines are based on observations made by Hassler & Moran. The solid line with the asterisks represents line widths obtained on 24th September 1992 in the centre of a coronal hole while the dashed line with the crosses represents line widths obtained on 23rd September 1992 at the edge of the same coronal hole.

acceleration. This is not surprising since all work provided by the extra Alfvén wave acceleration is converted to both heating and acceleration only in the subsonic part of the flow where the new pressure gradient leads to considerable compression of the flow. In this calculation this is negligible. In the outer regions (in this case for distances $r > 10\ \mathrm{R}_\odot$) momentum transfer to the flow leads mainly to acceleration rather than heating. In these outer supersonic regions, one would expect that the flow would cool down since density drops but because of the high velocities the plasma is quickly transported outwards and does not have enough time for cooling.

It has been suggested that the outer solar wind is heated by the dissipation of hydromagnetic turbulence and plasma instabilities. These cannot be included in this model. The role of turbulent dissipation in heating and accelerating the solar wind has been extensively studied in the past by Tu (1988), Hollweg (1986) and Hollweg & Johnson (1988). Goldstein (1996) has shown that nonlinear fluctuations in the solar wind at $0.3$ AU and beyond, which are driven by the expansion of the flow and the velocity gradients, are damped leading to heating of the wind. Verma et al. (1995) calculated the turbulent dissipation rates of incompressible hydromagnetic fluctuations and the resulting radial temperature evolution in the solar wind. For a complete description of magnetohydrodynamic turbulence and its effect on the solar wind the reader is refered to the review paper of Goldstein & Roberts (1995).

Recently, Orlando et al. (1996) modeled the propagation of three-dimensional, linear Alfvén waves in the solar corona and wind. They included physical effects like thermal conduction, radiative losses and heating as a phenomenological term

and calculated, temperature, density and velocity distributions extending from $1\,R_\odot$ to 1 AU. Their solar wind model was calculated by adjusting their base volumetric heating rate in each iteration step so that the wind temperature at 1 AU is $5 \times 10^5$ K. They showed that Alfvén waves can accelerate the wind by momentum deposition but their calculated wind velocity near the orbit of the Earth is of the order of $3000\,\mathrm{km\,s^{-1}}$ far higher than the observed values.

## 6. Conclusions

Our grid of 74 coronal models covers a wide array of potential solar wind solutions, even some that appear to be oscillating in the absence of a stable stationary solution. In comparing our results with observations we have focused on recent measurements of the temperature and emission measure in a coronal hole, deduced from X-ray observations with the Japanese satellite *Yohkoh* by Hara et al. (1994). We find that three of our models produce a good agreement with these observations for reasonable input parameters at the photospheric boundary.

All three models are close to the region in parameter space that does not give a stationary solution but a global relaxation oscillation.

In contrast to former models of coronal holes without acceleration by Alfvén waves, the velocity of the solar wind at the orbit of the Earth is very slow, only $10\,\mathrm{km\,s^{-1}}$. The solution finally goes supersonic through a critical point that lies at $1714\,R_\odot$. Earlier models of coronal holes based on older observations gave a final solar wind about half the observed velocity of 700 to $800\,\mathrm{km\,s^{-1}}$.

This means that the Alfvén waves are responsible for the whole acceleration of the wind to the observed velocities instead of just adding a contribution. A model including the acceleration of the wind by Alfvén waves gives a velocity at the Earth's orbit of $630\,\mathrm{km\,s^{-1}}$. These calculations show that the coronal temperature and the emission measure deduced by Hara et al. (1994), and the velocity of the wind at the Earth's orbit can be reproduced by a model in which the corona is heated by a flux of mechanical heating through the transition region of $2.1 \times 10^5\,\mathrm{erg\,cm^{-2}\,s^{-1}}$ with an average dissipation length of $0.1\,R_\odot$. The acceleration of the wind to observed velocities requires a flux of Alfvén waves of $1 \times 10^5\,\mathrm{erg\,cm^{-2}\,s^{-1}}$ at the base of the corona.

Our grid of models also reproduces solutions for the solar wind with a maximum temperature of about $1.4 \times 10^6 K$, which are in line with Skylab observations cited by Withbroe (1988), and with very recent observations by Foley et al. (1997) with *Yohkoh-SXT*, and Ko et al. (1997) with *Ulysses*. Previous models by Withbroe (1988) and others have been produced that fit these observational parameters, but these models are stationary, while ours is time-dependent. Thus our results also demonstrate the stability of these solutions.

*Acknowledgements.* We would like to thank G.C. Boynton, E.T. Rowe, U. Torkelsson, and G. Tóth for many useful discussions and comments.

## References

Alazraki G., Couturier P., 1971, A&A 13, 380
Balogh A.., Smith E.J., Tsurutani B.T., et al., 1995, Science 268, 1007
Belcher J.W., 1971, ApJ 168, 509
Belcher J.W., Davis Jr. L., 1971, J.Geophys.Res. 76, 3534
Bretherton F.P., 1970, in W.H. Reid (ed.), Mathematical Problems in the Geophysical Sciences pp 61
Dewar R.L., 1970, Phys. Fluids 13, 2710
Doschek G.A., Feldman U., 1977, ApJ 212, L143
Foley C.R., Culhane J.L., Acton L.W., 1997, ApJ 491, 933
Goldstein M.L., 1996, in D. Winterhalter, J.T. Gosling, S.R. Habbal, W.S. Kurth and M. Neugerbauer (eds.), Solar Wind Eight AIP conference Proceedings 382, Woodbury, New York, pp 239
Goldstein M.L., Roberts D.A., 1995, ARA&A 33, 283
Guhathakurta M., Rottman G.J., Fisher R.R., Orrall F.Q., Altrock R.C., 1992, ApJ 388, 633
Hara H., Tsuneta S., Acton L.W., et al., 1994, PASJ 46, 493
Hammer R., 1982a, ApJ 259, 767
Hammer R., 1982b ApJ 259, 779
Hammer R., 1983, Adv.Space Res. 2, 261
Hartmann L., MacGregor K.B., 1980, ApJ 242, 260
Hartmann L., MacGregor K.B., 1982, ApJ 257, 264
Hassler D.M., Moran T.G., 1994, Space Sci. Rev. 70, 373
Hearn A.G., Vardavas I.M., 1980, A&A 98, 230
Hearn A.G., Kuin N.P.M., Martens P.C.H., 1983, A&A 125, 69
Heyvaerts J., 1996, in C. Chiuderi and G. Einaudi (eds.), Plasma Astrophysics, Springer-Verlag, Heidelberg, pp 31
Hirsch C., 1990, Numerical computation of internal and external flows, John Wiley & Sons, Chichester
Hollweg J.V., 1986, J.Geophys.Res. 91, 4111
Hollweg J.V., Johnson W., 1988, J.Geophys.Res. 93, 9547
Holzer T.E., 1979, in E.N. Parker, C.R. Kennel and L.J. Lanzelloti (eds.), Solar System Plasma Physics, North Holland Publishing Company, Amsterdam, pp 101
Hundhausen A.J., 1977, in J.B. Zirker (ed.), Coronal Holes and High Speed Wind Streams, Colorado Associated University Press, Boulder, pp 225
Jacques S.A., 1977, ApJ 215, 942
Jacques S.A., 1978, ApJ 226, 632
Kelly D.R.C., Korevaar P., 1995, A&A 296, 418
Ko Y-K, Fisk L.A., Geiss J., Gloeckler G., Guhathakurta M., 1997, A&A 171, 345.
Korevaar P., Hearn A.G., 1989a, A&A 220, 177
Korevaar P., Hearn A.G., 1989b, A&A 224, 141
Korevaar P., Van Leer B., 1988, A&A 200, 153
Krieger A.S., Timothy A.F., Roelof E.C., 1973, Solar Phys. 29, 505
Mariska J.T., 1978, ApJ 225, 252
Maxson C.W., Vaiana G.S., 1977, ApJ 215, 919
McWhirter R.W.P., Thonemann P.C., Wilson R., 1975, A&A 40, 63
McWhirter R.W.P., Thonemann P.C., Wilson R., 1977, A&A 61, 859
Munro R.H., Withbroe G.L., 1972, ApJ 176, 511
Nolte J.T., Krieger A.S., Timothy A.F., et al., 1976, Solar Phys. 46, 303
Ogawara Y., Takano T., Kato T., et al., 1991, Solar Phys. 136, 1
Orlando S., Lou Y.-Q., Rosner R., Peres G., 1996, J.Geophys.Res. 101, 24443
Parker E.N., 1958, ApJ 128, 664
Parker E.N., 1965, Space Sci. Rev. 4, 666
Phillips J.L., Bame S.J., Feldman W.C., et al., 1995, Science 268, 1030
Pneuman G.W., 1986, Space Sci. Rev. 43, 105
Spitzer L., 1956, Physics of Fully Ionized Gases, Interscience, New York

Tsuneta S., Acton L., Bruner M., et al., 1991, Solar Phys. 136, 37
Tu C-Y., 1988, J.Geophys.Res. 93, 7
Ulmschneider P., 1970, Solar Phys. 12, 403
Van Leer B., 1982, Lect.Notes Phys. 170, 507
Verma M.K., Roberts D.A., Goldstein M.L., 1995, J.Geophys.Res. 100, 19839
Withbroe G.L., 1988, ApJ 325, 442